6. The Squirrel-Cage Induction Machine

Slipring-induction machines do not only have advantages, but also a number of disadvantages: Manufacturing of the wound rotor is expensive, the rotor is not very robust at high speed, the carbon brushes of the sliding contacts need maintenance, and the starting-torque without use of external resistances is rather small. Shortly before the beginning of the 20th century, *Michael von DOLIVO-DOBROWOLSKI*, who **studied** at *TH Darmstadt* and later on was a research assistant, made the **squirrel-cage induction machine** (Fig. 6.1a), that had been invented by *Prof. FERRARIS*, to become a technically useful product. Here, massive, blank copper bars are embedded into the rotor slots and are shorted at their ends by a soldered copper ring. Squirrel-cages made from die-cast aluminium are also commonly used, notably at smaller power (Fig. 6.1b). Two neighbouring bars form, together with the corresponding ring section, a rotor mesh. If a slip different from zero occurs between the rotor speed and the speed of the stator rotating field, the stator rotating field induces a voltage in this mesh. The resulting rotor bar current generates, together with the stator air gap field – as in the case of the slipring-induction machine – the electromagnetic torque. Thus, the working characteristics of squirrel-cage and slipring-induction machines are basically the same. Hence, the equivalent circuit, the space vector diagram, power flow scheme and circle diagram derived for slipring induction machines remain valid for squirrel-cage induction machines. However, some qualitative and quantitative differences are noticeable. They are discussed in the present chapter.

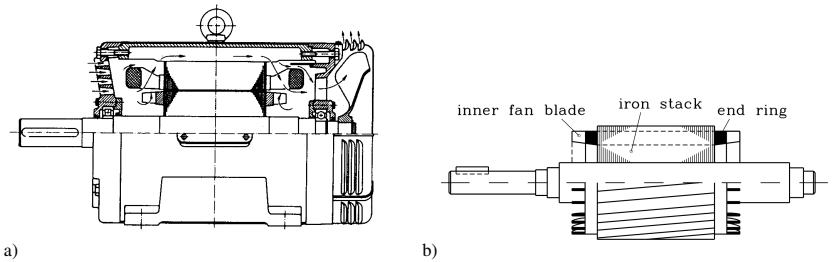

Fig. 6.1: a) Squirrel-cage induction machine (here with internal air cooling), b) typical die-cast squirrel-cage (skewed slots to reduce parasitic effects of field harmonics, cast-on "inner fan blades" at the rings)

6.1 Currents and Voltages in the Squirrel-Cage

a) Induced Voltages in the Bars:

The **fundamental of the stator rotating field** (Fig. 6.2a) with the amplitude $\hat{B}_{\delta,s}$ moves with the velocity v_{syn} in the air gap, whereas the squirrel-cage rotates with the surface velocity v_m that corresponds to the rotor speed n. Hence, it moves relative to the stator rotating field $B_{\delta,s}$ with the speed $sv_{syn} = v_{syn} - v_m$. A "rotor mesh" given by two bars, distanced by τ_p, is linked with a flux with the amplitude:

$$\boxed{\Phi = \frac{2}{\pi}\tau_p l \hat{B}_{\delta,s}} \qquad (6.1)$$

The flux changes with the rotor frequency $f_r = s f_r$ and induces a mesh voltage with an amplitude given by (6.2).

$$\hat{U}_{i,c} = 2\pi \cdot s f_s \cdot \frac{2}{\pi}\tau_p l \hat{B}_{\delta,s} = s \cdot 2 \cdot (2 f_s \tau_p) \cdot l \cdot \hat{B}_{\delta,s} = s \cdot 2 \cdot v_{syn} \cdot l \cdot \hat{B}_{\delta,s} \quad . \qquad (6.2)$$

Half of the voltage $\hat{U}_{i,c}$ occurs as **bar voltage** $\hat{U}_{i,bar} = \hat{U}_{i,c}/2$:

$$\boxed{\hat{U}_{i,bar} = s v_{syn} \hat{B}_{\delta,s} l} \qquad (6.3)$$

As two adjacent bars are spatially displaced by the rotor slot pitch τ_{Qr}, the two sinusoidal voltages are displaced by the **rotor slot angle**:

$$\alpha_{Qr} = \frac{2\pi p}{Q_r} \qquad (6.4)$$

This angle corresponds to the time the field wave needs to pass the distance τ_{Qr}. If the voltage phasors of all bars are drawn in the complex plane, a **regular bundle of voltage phasors** is obtained (Fig. 6.2).

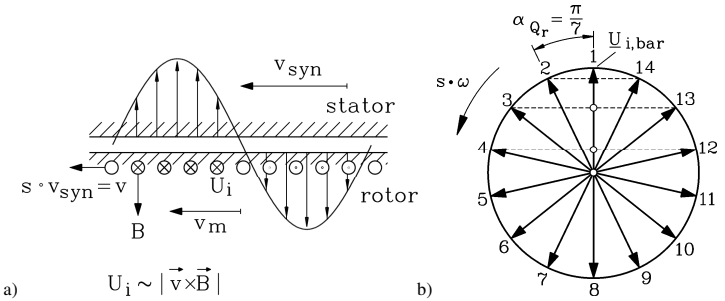

Fig. 6.2: a) The fundamental of the stator field induces an electric voltage in each bar that is phase shifted towards the voltage of the neighbouring bar by α_{Qr}, b) regular bundle of voltage phasors of a squirrel-cage rotor with $Q_r/p = 14$ bars/pole pair. The voltage phasors of two neighbouring bars are phase shifted by the rotor slot angle $\pi/7$. In a 4 pole machine, the voltages in bar 1 and 15, 2 and 16 etc. have the same phase angle, respectively.

b) Bar Currents, Bar Forces and Torque:

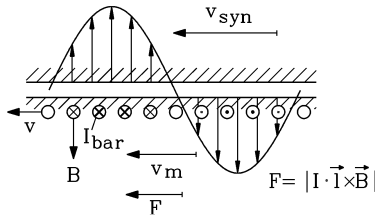

Fig. 6.3: **Torque generation** of a squirrel-cage induction machine. At small slip s, the sinusoidal fundamental of the rotor electric loading and of the stator field are spatially almost in phase and generate *LORENTZ* forces per bar. At small slip s, force and torque increase linear with s, because it is $F_{bar} \sim I_{bar} \sim U_{i,bar} \sim s$ (see *KLOSS*'s formula for small values of s!).

At small slip s, the rotor frequency $f_r = sf_s$ is very small, hence, the reactance of the bars is much smaller than the *OHM*ic resistance of the bars. Therefore, the bar currents are almost in phase with the induced voltage. Together with the stator field wave, they generate a ***LORENTZ* force in each bar (6.5)**. Each of the forces in the bars generates – together with the lever $d_r/2$ – an electromagnetic torque M_e.

$$\boxed{\hat{F}_{bar} = \hat{I}_{bar} l \hat{B}_{\delta,s}} \tag{6.5}$$

The **rotor bar currents** are caused by the voltages of Fig. 6.2b, hence, they form a **regular bundle of current phasors** (Fig. 3.5b) that generates a rotating field wave in the air gap (Fig. 3.6). The fundamental of this wave rotates with the speed sn_{syn} with respect to the rotor, and with $n + sn_{syn} = n_{syn}$ with respect to the stator. Hence, the rotor fundamental moves as fast as the stator wave. Rotor and stator rotating field may be added and give the resultant sinusoidal air gap field, which rotates with n_{syn}.

c) Ring Section Currents:
Ring section currents flow in the individual **ring sections** (Fig. 6.4). The ring section current – e.g. between bars no. 2 (bar current I_2) and no. 3 (bar current I_3) – has the amplitude I_{23}. Due to reasons of symmetry, the time phasors of the **ring section currents in the different ring sections** form – in the same way as the phasors of the bar currents – a regular bundle of current phasors. According to 2nd *KIRCHHOFF*'s law, it is, e.g. for bar no. 2 at the junction of the bar to the two neighbouring ring sections "12" and "23":

$$\underline{I}_{12} + \underline{I}_2 - \underline{I}_{23} = 0 \tag{6.6}$$

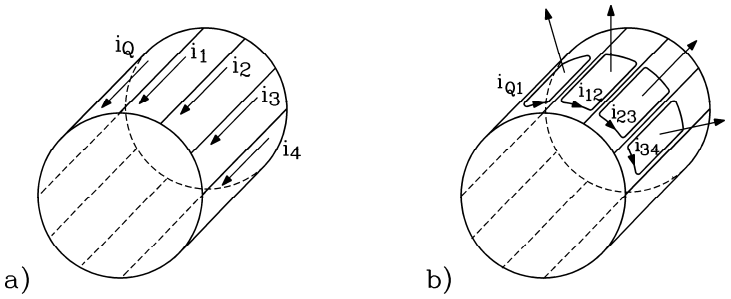

Fig. 6.4: Current distribution in a squirrel-cage: a) bar currents, b) currents in the ring sections

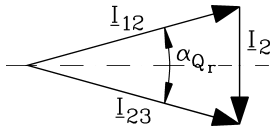

Fig. 6.5: 2nd *KIRCHHOFF*'s law for the currents of two ring sections $\underline{I}_{12}$ and $\underline{I}_{23}$ and the bar current $\underline{I}_2$.

The bar current is derived from Fig. 6.5:

$$I_2 = 2I_{12}\sin(\alpha_{Qr}/2) \quad \Rightarrow \quad I_{bar} = 2I_{ring}\sin(p\pi/Q_r) \tag{6.7}$$

Therefore, the *OHM*ic resistance of the ring section ΔR_{ring} can be simply added as a **series resistance** ΔR^*_{ring} to the resistance of the bar R_{bar} via calculation of the total copper losses in the squirrel-cage.

$$P_{Cu,r} = Q_r R_{bar} I^2_{bar} + 2Q_r \Delta R_{ring} I^2_{ring} = Q_r (R_{bar} + \Delta R^*_{ring}) I^2_{bar} \quad \Rightarrow$$

$$\boxed{\Delta R^*_{ring} = \Delta R_{ring} \frac{1}{2\sin^2(\pi p/Q_r)}} \tag{6.8}$$

d) Current and Voltage Transfer Ratio of a Squirrel-Cage Winding:
As the bar currents of the individual bars are different by the phase shift, each bar is considered as a **single phase**. Each bar forms half of a winding, the number of turns per phase N_r is ½ and the number of phases m_r is Q_r. The winding factor $k_{w,r}$ of this simple winding phase is $k_{wr} = 1$, because short-pitching and more than one coil per pole and phase do not exist. The fundamental of the magnetic voltage (m.m.f.) of such a "multiple phase" cage was derived in Chapter 3. The rotor field fundamental is derived for $\mu_{Fe} \to \infty$:

$$\hat{V}_{\delta,r} = \frac{\sqrt{2}}{\pi}\frac{m_r}{p} N_r k_{w,r} I_{bar} \quad \Rightarrow \quad \hat{B}_{\delta,r} = \mu_0 \frac{\hat{V}_{\delta,r}}{\delta} \tag{6.9}$$

If the same field shall be excited by the stator winding, the stator winding must excite the same magnetic voltage, hence, it must carry the **equivalent current** I'_r. Thereby, the rotor bar current converted to the stator side is derived:

$$\hat{V}_{\delta,r} = \hat{V}_{\delta,s} = \frac{\sqrt{2}}{\pi}\frac{m_s}{p} N_s k_{w,s} I'_r$$

$$I'_r = I_{bar}\frac{N_r}{N_s}\cdot\frac{k_{w,r}}{k_{w,s}}\cdot\frac{m_r}{m_s} = I_{bar}\frac{Q_r}{2N_s k_{w,s} m_s} \Leftrightarrow I'_r = \frac{I_{bar}}{\ddot{u}_I} \tag{6.10}$$

With squirrel-cage induction motors, voltage and current transfer ratio are therefore **different**:

$$\boxed{\ddot{u}_U = \frac{k_{w,s}N_s}{k_{w,r}N_r}} \qquad \boxed{\ddot{u}_I = \frac{k_{w,s}N_s m_s}{k_{w,r}N_r m_r} = \frac{2k_{w,s}N_s m_s}{Q_r}} \tag{6.11}$$

$$\boxed{\frac{I_r}{\ddot{u}_I} = \frac{I_{bar}}{\ddot{u}_I} = I'_r} \qquad \boxed{\ddot{u}_U U_r = U'_r} \tag{6.12}$$

It must be noted, that the mutual inductances M_{sr} and M_{rs} **are different** ($M_{sr} \neq M_{rs}$) due to $m_s \neq m_r$, which is a difference to slipring induction motors. The stator excited field, which is proportional to the number of stator phases m_s, induces the rotor. Therefore, it is:

$$M_{sr} = \mu_0 N_r k_{w,r} N_s k_{w,s} \cdot \frac{2m_s}{\pi^2} \cdot \frac{l\tau_p}{p\delta} \tag{6.13}$$

Vice versa, the rotor excited field, which is proportional to the number of rotor phases m_r, induces the stator. Therefore, it is:

$$M_{rs} = \mu_0 N_s k_{w,s} N_r k_{w,r} \cdot \frac{2m_r}{\pi^2} \cdot \frac{l\tau_p}{p\delta} \tag{6.14}$$

Hence, it is:

$$\ddot{u}_U \cdot M_{sr} = \frac{k_{w,s}N_s}{k_{w,r}N_r} \cdot \mu_0 \cdot N_r k_{w,r} \cdot N_s k_{w,s} \cdot \frac{2m_s}{\pi^2}\frac{l\tau_p}{p\delta} = \mu_0 N_s^2 k_{w,s}^2 \cdot \frac{2m_s}{\pi^2}\frac{l\tau_p}{p\delta} = L_{sh} \tag{6.15}$$

$$\ddot{u}_I \cdot M_{rs} = \frac{k_{w,s}N_s m_s}{k_{w,r}N_r m_r} \cdot \mu_0 \cdot N_s k_{w,s} \cdot N_r k_{w,r} \cdot \frac{2m_r}{\pi^2}\frac{l\tau_p}{p\delta} = \mu_0 N_s^2 k_{w,s}^2 \cdot \frac{2m_s}{\pi^2}\frac{l\tau_p}{p\delta} = L_{sh} \tag{6.16}$$

The self-inductance of the rotor air gap field is, converted to stator winding data:

$$\ddot{u}_U \ddot{u}_I L_{rh} = \left(\frac{k_{w,s}N_s}{k_{w,r}N_r}\right)^2 \frac{m_s}{m_r} \cdot \mu_0 N_r^2 k_{w,r}^2 \cdot \frac{2m_r}{\pi^2}\frac{l\tau_p}{p\delta} = \mu_0 N_s^2 k_{w,s}^2 \cdot \frac{2m_s}{\pi^2}\frac{l\tau_p}{p\delta} = L_{sh} \tag{6.17}$$

Resistance and inductance are converted as follows:

$$\boxed{R'_r = \ddot{u}_U \ddot{u}_I R_r} \qquad \boxed{L'_{r\sigma} = \ddot{u}_U \ddot{u}_I L_{r\sigma}} \qquad \boxed{\ddot{u}_U M_{sr} = \ddot{u}_I M_{rs} = \ddot{u}_U \ddot{u}_I L_{rh} = \underline{\underline{L_h}}} \tag{6.18}$$

The **voltage equations** of Chapter 5 are converted with $\ddot{u}_U$ ***and*** $\ddot{u}_I$:

$$\underline{U}_s = j\omega_s \cdot \ddot{u}_I M_{rs} \cdot (\underline{I}_r / \ddot{u}_I) + j\omega_s L_h \underline{I}_s + j\omega_s L_{s\sigma} \underline{I}_s + R_s \underline{I}_s \tag{6.19}$$

$$j\omega_r \ddot{u}_U M_{sr} \underline{I}_s + j\omega_r \ddot{u}_U \ddot{u}_I L_{r,h} \cdot (\underline{I}_r / \ddot{u}_I) + j\omega_r \ddot{u}_U \ddot{u}_I L_{r\sigma} \cdot (\underline{I}_r / \ddot{u}_I) + \ddot{u}_U \ddot{u}_I R_r \cdot (\underline{I}_r / \ddot{u}_I) = 0\,. \tag{6.20}$$

As a result, the same voltage equations as for the slipring induction machine are obtained:

$$\underline{U}_s = j\omega_s L_h \underline{I}'_r + j\omega_s L_h \underline{I}_s + j\omega_s L_{s\sigma} \underline{I}_s + R_s \underline{I}_s \tag{6.21}$$

$$0 = js\omega_s L_h \underline{I}_s + js\omega_s L_h \underline{I}'_r + js\omega_s L'_{r\sigma} \underline{I}'_r + R'_r \underline{I}'_r \tag{6.22}$$

Divided by s, they are expressed by reactances:

$$\boxed{\underline{U}_s = R_s \underline{I}_s + jX_{s\sigma} \underline{I}_s + jX_h(\underline{I}_s + \underline{I}'_r)} \qquad \boxed{0 = \frac{R'_r}{s} \underline{I}'_r + jX'_{r\sigma} \underline{I}'_r + jX_h(\underline{I}_s + \underline{I}'_r)} \tag{6.23}$$

Remark: With slipring rotors, it is $\ddot{u}_U = \ddot{u}_I$, because it is normally $m_s = m_r$.

Result:
Considering the differences shown above, the validity of the T-equivalent circuit of the induction machine of Chapter 5 has been shown. Hence, the squirrel-cage induction machine can be calculated in the same way as a slipring induction machine.

6.2 Current Displacement in the Rotor Bars

The rotor bars have a much larger cross sectional area A_{bar} than the wire wound stator coils. Fig. 6.6 shows a rectangular bar (**"deep bar"**). Assuming that the current density (r.m.s. value) (6.24)

$$J_{bar} = \frac{I_{bar}}{A_{bar}} \tag{6.24}$$

is evenly distributed over the bar cross sectional area, the slot leakage field can easily be calculated. The field lines encircle the exciting bar current. Because of the higher magnetic conductivity of the iron, the field lines are almost only inside the rotor lamination, only crossing the slot width b_r, and entering the iron almost perpendicularly (Fig. 6.6a). A co-ordinate system is given to the slot (origin at slot base, y-axis across the slot, x-axis along the longitudinal axis). The iron field H_{Fe} is neglected when compared with the slot field H_Q, because of the high permeability of iron. Applying *AMPERE*'s law and assuming that the curve C equals a single field line that crosses the slot at point x, equation (6.25) is obtained: The slot flux density $B_Q = \mu_0 \cdot H_Q$ **increases linear** with the coordinate x along height of the bar. So the rotor slot stray field and the **slot leakage** inductance **increase with bar height**.

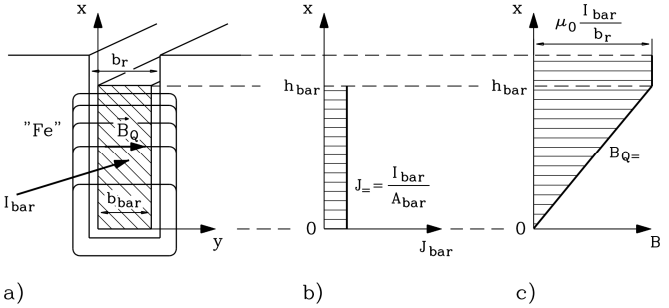

Fig. 6.6: Deep bar rotor in rectangular rotor slot: a) flux plot of the slot leakage field, b) assumed uniform distribution of the current density in the bar, c) distribution of the slot flux density

The slot field is constant in the region of the "slot end", where the bar ends and is fixed by a wedge; here no current flows.

$$\oint_C \vec{H} \cdot d\vec{s} = H_Q(x) \cdot b_r = J \cdot x \cdot b_{bar} \quad \Rightarrow$$

$$B_Q(x) = \mu_0 J \frac{x \cdot b_{bar}}{b_r} = \mu_0 \frac{I_{bar}}{b_r} \cdot \frac{x}{h_{bar}} \qquad 0 \le x \le h_{bar} \tag{6.25a}$$

$$B_Q = \mu_0 \frac{I_{bar}}{b_r} \qquad h_{bar} \le x \le h_Q \tag{6.25b}$$

This **slot flux density B_Q** pulsates with rotor frequency and penetrates the bar along its broadside. Therefore, the bar is a "short-circuit loop" for the pulsating slot field (Fig. 6.7), and the slot field induces an eddy current field $\vec{E}$ according to *FARADAY*'s law of induction. Due to the negative sign of $u_i = -d\Phi/dt$, it causes an eddy current in the bar that results in a magnetic self-field $B_{Q,Ft}$ that acts against the primary slot field (*LENZ*'s law, Fig. 6.7). Accordingly, the **eddy current** I_{Ft} (Ft: *FOUCAULT*) causes a bar current I_{bar} that flows in the upper region of the bar IN the direction of the bar current, and in the bottom region of the bar CONTRARY to the bar current. Thereby, an uneven current density is obtained in the rotor bar which is larger in the upper than in the lower region of the bar. The current is "displaced" from the slot bottom to the slot opening (**current displacement, skin effect**).

This effect **increases** with
- increasing rotor frequency f_r, because the induced voltage increases,
- increasing electric conductivity κ of the bar, because the eddy current increases,
- increasing height of the bar h_{bar}, because the flux through the "short-circuit loop" increases,
- increasing permeability μ of the conductor (as long as $\mu << \mu_{Fe}$ is true), because the leakage field B_Q, that induces the eddy current, increases.

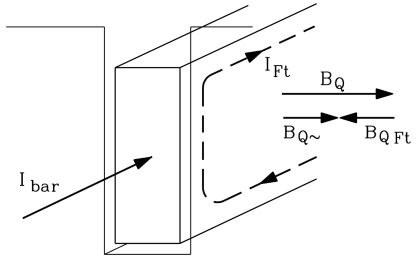

Fig. 6.7: Eddy current I_{Ft} in a deep bar excited by an a.c. slot flux density B_Q that pulsates with rotor frequency

The **resulting current density distribution** $J(x)$ can be calculated relatively easily by solving *MAXWELL*'s equations for the geometry shown in Fig. 6.6. Fig. 6.8 shows the result for 0 Hz and 50 Hz rotor frequency qualitatively. The resulting slot field $B_{Q\sim}$ is weakened by the reacting self-field of the eddy current $B_{Q\,Ft}$, as shown in Fig. 6.7. Therefore, it is smaller at 50 Hz than at 0 Hz rotor frequency.

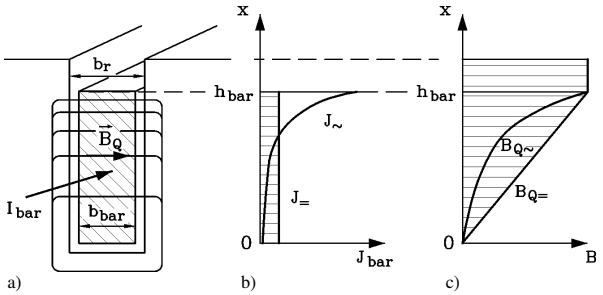

Fig. 6.8: **Single sided current displacement in a rectangular bar** at 50 Hz when compared to 0 Hz (dc current). a) Cross section of slot and bar, b) distribution of the current density, c) distribution of the slot flux density. At dc current (=), the slot field does not pulsate and no eddy currents are induced. Current displacement does not take place. At 50 Hz (~), the current density at the bar upper edge increases because of current displacement.

From Fig. 6.8, it is derived:
- As the larger part of the bar current flows only in the upper section of the bar, only a part of the cross sectional area of the bar is used. Hence, the electrically effective *OHM*ic resistance of the bar increases. **The "ac resistance" $R_{bar\sim}$ is larger than the dc resistance $R_{bar=}$.**

$$R_{bar\sim} = k_R R_{bar=} > R_{bar=} \tag{6.26}$$

- The slot leakage inductance decreases because of the weakening of the slot leakage field. **The ac inductance $L_{bar\sim}$ is smaller than the dc inductance $L_{bar=}$.**

$$L_{\sigma,bar\sim} = k_L L_{\sigma,bar=} < L_{\sigma,bar=} \tag{6.27}$$

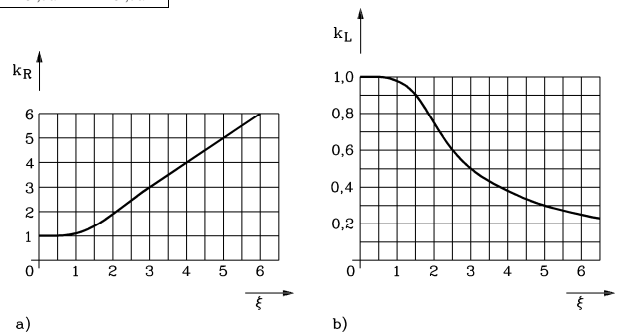

Fig. 6.9: Current displacement factors k_R (increase of the bar resistance) and k_L (decrease of the slot leakage inductance) of a "deep bar" as a function of the **"reduced" conductor height** ξ

By solving *MAXWELL*'s equations, it can be shown that the coefficients k_R, k_L for a rectangular bar can be expressed as a function of a **single** dimensionless parameter ξ, which is the **"reduced" conductor height** that contains all parameters of influence (Fig. 6.9) (Derivation, see the lecture *"Large Generators and High Power Drives"*).

$$\xi = h_{bar}\sqrt{\pi f_r \mu \kappa \frac{b_{bar}}{b_r}} \tag{6.28}$$

$$k_R = \xi \frac{\sinh(2\xi)+\sin(2\xi)}{\cosh(2\xi)-\cos(2\xi)} \tag{6.29}$$

$$k_L = \frac{3}{2\xi}\cdot\frac{\sinh(2\xi)-\sin(2\xi)}{\cosh(2\xi)-\cos(2\xi)} \tag{6.30}$$

Example 6.2-1:
At 75°C, the value of the electric conductivity of a copper bar is $\kappa_{Cu} = 50\cdot10^6$ S/m. With $b_{bar} = b_r$, $\mu_{Cu} = \mu_0 = 4\pi\cdot10^{-7} Vs/(Am)$ and a chosen rotor frequency of $f_r = 50$ Hz, the current displacement factor for the resistance is $k_R = h_{bar}^{[cm]}$. Hence, at a bar height of $h_{bar} = 3$ cm, it is $\xi = 3$ and – according to Fig. 6.9 – the effective resistance is tripled. The inductance is reduced to 50%.

6.3 Design of Squirrel-Cages to Increase the Breakaway Torque

The current displacement of grid-operated induction machines at low speed (hence, high rotor frequencies) causes an increase of the rotor resistance. This is used to increase the starting torque. It has been shown (Chapter 5) that an increase of the rotor losses causes an increase of the breakaway torque M_1.

$$M_e(s) = \frac{P_\delta}{\Omega_{syn}} = \frac{P_{Cu,r}/s}{\Omega_{syn}} \quad \Rightarrow \quad M_1 = M_e(s=1) = \frac{P_{Cu,r}}{\Omega_{syn}} \tag{6.31}$$

Therefore, special bar shapes have been designed to obtain a high breakaway torque (Fig. 6.10).

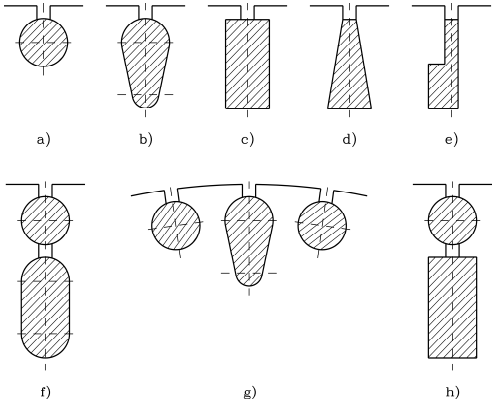

Fig. 6.10: Bar shapes of single and double squirrel-cage rotors: a) round bar, b) oval bar, c) deep bar, d) keyed bar (wedge or tapered deep bar), e) L bar, f) and h): double bar, g) staggered-slot rotor

a) Bars with Small Current Displacement:
The **round bar** has a small bar height. Hence, the influence of current displacement is only small. Due to its shape, the rotor tooth between two bars has a small cross section (magnetic bottleneck due to squeezing of flux lines, high flux density, high iron saturation), which is disadvantageous. The tooth between two **oval bars** has parallel sides and the squeezing of the flux lines is avoided. The cross section increases towards the slot opening, and the influence of current displacement is much smaller than in the case of a deep bar. Round and oval bars are not suited to obtain a high breakaway torque, but are used for **inverter operation**. At inverter operation, the current is no longer sinusoidal. Beside the current fundamental, current harmonics with higher frequencies occur. Therefore, already at rated operation, high rotor frequencies are excited that cause current displacement and therefore increased copper losses. In this case, current displacement shall be avoided to reduce the losses at rated operation. Breakaway torque is not of significance, because the machine is frequency controlled and can thereby be started with rated torque (see Chapter 7).

b) Bars with High Current Displacement:
The **keyed bar (wedge bar)** narrows towards the slot opening. Therefore, less cross-sectional area is available for the cur-rent displaced to the slot opening than in the case of a **deep bar**. Therefore, the current displacement has a stronger effect than in the case of a deep bar, and the breakaway torque is larger. In the case of a **double squirrel-cage rotor**, the bar is divided into two bars with different material. The top bar close to the air gap has a small cross sectional area and is made from bronze. Current displacement at $s = 1$ leads to current flow mainly in the upper bar, where high losses occur due to an increased resistance. This results in a high breakaway torque. The bottom bar is made from copper and has a large cross sectional area. Therefore, it has a low resistance. At rated operation, where hardly any current displacement occurs and the current divides according to the *OHM*ic dc resistances of top and

bottom cage, the current flows mainly in the bottom bar, causing only small losses. Therefore, the cage with the top bars is also called **starting cage**, the bottom cage **operation cage**.

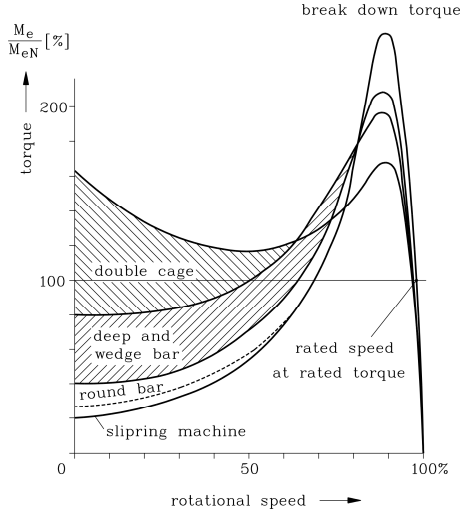

Fig. 6.11: Typical torque characteristics of induction machines

The torque of $M(n)$-characteristics of induction machines with different rotor cages (Fig. 6.11) is referred to the rated torque of the machine, and the speed is referred to synchronous speed, in order to compare machines of different size in one diagram. **Slip-ring induction motors** without starting resistors have a small breakaway torque (typically 20% of the rated torque for rated power from 1 kW up to 100 kW). The rotor winding of smaller machines consists of coil wires with a small cross section in which eddy currents cannot occur. Therefore, it is almost free of current displacement. The same is true for **round bar squirrel-cage rotors**. **Wedge bar and deep bar squirrel-cage machines** have a significantly higher breakaway torque (40% to 80%), whereas the breakaway of **double squirrel-cage machines** values up to 160% and can even exceed the breakdown torque.
For slip values $s_b > s > 0$ the rotor frequency is small; the current displacement effect vanishes. According to Fig. 6.6 the rotor slot leakage inductance increases with increasing bar height (without current displacement effect), and so does the leakage coefficient σ. Hence the break-down torque, referred to the rated torque $M_b/M_N \sim (1 - \sigma)/\sigma$ (Chapter 5) is smaller for rotors witch increased bar height, which is clearly visible in Fig. 6.11.

c) Double Squirrel-Cage Rotor:
Starting cage and operating cage act electrically as parallel connection of two rotor circuits, as shown in the T-equivalent circuit of Fig. 6.12. The leakage field of the upper bar closes via the iron, thereby enclosing the lower bar. Hence, the two bars are linked and the corresponding leakage reactance $X'_{r,\sigma o}$ concerns both upper and lower bar. The leakage field of the lower bar closes via the stray gap and the iron only around the lower bar itself, hence the reactance $X'_{r,\sigma u}$ is only effective for the operation cage. Using this equivalent circuit, the current consumption for each slip can easily be determined, and thereby the power conversion and the generated torque is calculated. Qualitatively, the operational characteristic at neglected stator resistance can be estimated as follows:

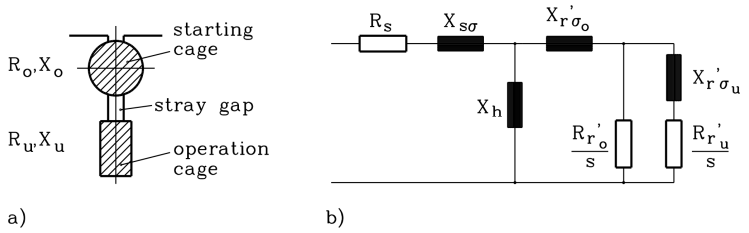

Fig. 6.12: Double squirrel-cage machine: a) cross sectional area of a rotor slot, b) simplified T-equivalent circuit

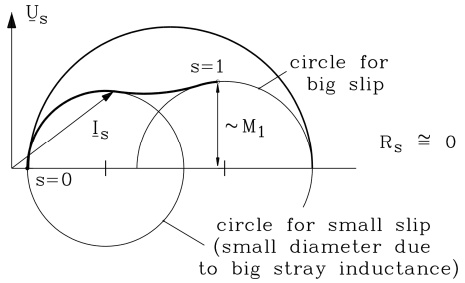

Fig. 6.13: **Double squirrel-cage machine**: simplified stator current locus diagram for starting and operation cage ($R_s \cong 0$).

At large slip ($s >> 1$), the resistances R'_{ro}/s, R'_{ru}/s can be neglected when compared with $X'_{r,\sigma u}$. Then, because of the relatively high $X'_{r,\sigma u}$, the current flows only in the starting cage with its small leakage inductance. This results in a large circle diameter of the current locus diagram. As a rough approximation, the circle diagram is a large circle at big slip ($s \to \infty$), and a circle that converges towards the large circle at decreasing slip (s~1).

At small slip ($s << 1$), the resistances R'_{ro}/s, R'_{ru}/s dominate over $X'_{r,\sigma u}$. Due to $R'_{ro} >> R'_{ru}$, the current flows only in the operation cage. The corresponding circle diagram has a significantly smaller circle diameter, because of the larger rotor leakage ($X'_{r,\sigma u} + X'_{r,\sigma o} >> X'_{r,\sigma o}$) and hence the larger leakage coefficient σ. The centres of the circles are on the negative imaginary axis that is also the "torque line", because of the neglected stator resistance. The real current component of the stator current (vertical component in Fig. 6.13) is directly proportional to the electromagnetic torque, resulting directly in the **"saddle"** shaped torque characteristic with a saddle at about $s = 0.5$ (Fig. 6.13).

d) Typical Breakaway Currents and Torques:

The breakaway current I_I (starting current) of squirrel-cage motors is about 4 to 7 times as large as the rated current I_N. The larger value occurs with larger motors and is strongly inductive. The breakaway torque M_I of large motors ($P_N \geq$ 1MW) values only 0.6 to 1.2 times the rated torque. As high power working machines – turbo compressors, pumps, fans, coal mills, ... – are often started at reduced load, hence with closed valves, the breakaway torque of the motors is often large enough to allow safe running-up. Industrial motors with small power ($P_N \leq$ 200 kW) which have internationally standardised dimensions of the mechanical connections (shaft height, length and diameter of shaft ends and feather key, flange dimensions at flange motors) and power levels (**"standard motors"**), have larger per unit breakaway torque, notably if designed with double squirrel-cage rotors, but also relatively high starting currents (up to 7 times the rated current).

6.4 Deviations of the Circle Diagram

a) Influence of Current Displacement on the Stator Current Locus Diagram:

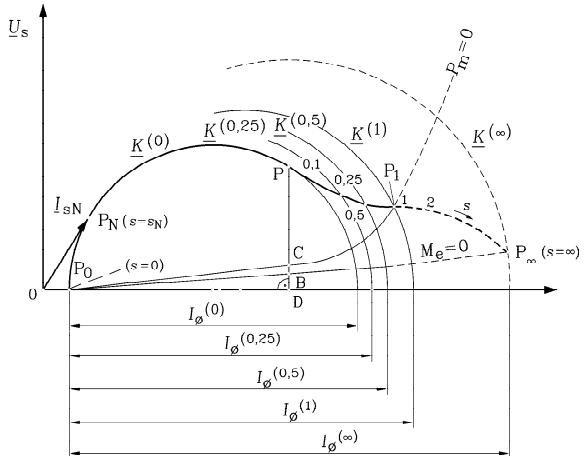

Fig. 6.14: Due to the current displacement, the locus diagram $\underline{I}_s(s) = \underline{K}(s)$ of the stator current of a deep bar motor is **no longer a circle**.

It is obvious from Fig. 6.13 that the stator current locus diagram of double squirrel-cage rotors is NO LONGER a circle diagram. However, also in the case of motors with one deep bar squirrel-cage, the **current locus diagram IS NO LONGER a circle**. It was shown (Section 6.2) that the current displacement causes an **increase of the rotor resistance** and a **decrease of the rotor inductance**. It was shown with slipring machines that a change of the rotor resistance does not change the circular shape of the current locus diagram. Only the slip scaling of the circle is changing ("shear" of the $M(n)$-characteristic). However, a **decrease of the leakage inductance** increases *BLONDEL*'s leakage coefficient. Thereby, the diameter of the circle diagram increases at large slip values, as a high rotor frequency leads to a high current displacement and the diagram is "inflated" (Fig. 6.14). This is the graphical explanation for the increase of the torque: The distance between the "torque line" (which is now also curved) and the locus P_1 which is proportional to the torque, increases. In practical applications, the torque is determined numerically from the equivalent circuit for variable rotor parameters for each slip value. No "circle diagram" is used any longer.

b) Influence of the Saturation of the Main Field:

Example 6.4-1:

Four-pole induction machine: $2p = 4$, $q_s = 5$, $Q_s = 60$, $Q_r = 44$

Stator: rectangular slots, shaped wire, two layer high voltage winding

Rotor: tapered deep-bar squirrel-cage rotor

Calculation of the (two dimensional) magnetic field using the finite element method:
a) **no-load** (rotor at zero current, Fig. 6.15a), rated voltage,
b) **breakaway point** (s = 1, Fig. 6.15b), rated voltage.

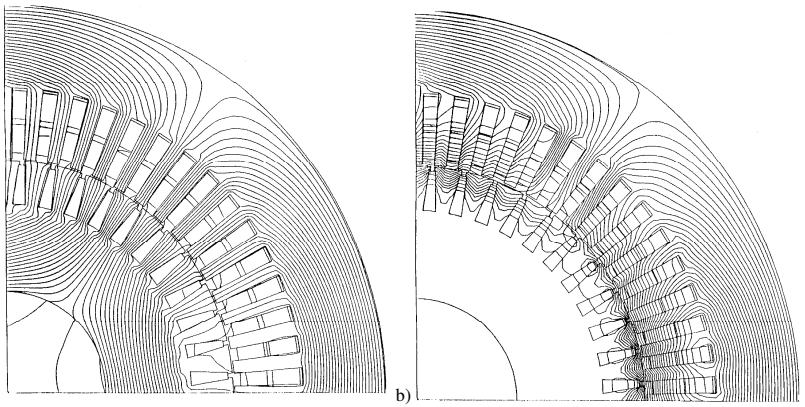

Fig. 6.15: Numerically calculated two-dimensional magnetic flux density B of an induction machine a) at no-load and rated voltage (s = 0, rotor at zero current), b) at breakaway torque s = 1 and rated voltage

At **no-load**, only the magnetising current flows in the stator winding. It generates the magnetising field in the air gap so that the voltage induced in the stator winding balances the line voltage. The field lines have to squeeze in the teeth. Therefore, for an air gap field density of 1 T, the magnetic field density in the teeth reaches values as high as 1.8 T to 2 T. Above typically 1.5 T the iron saturates, and the *m.m.f.* of the stator winding V_s is not only used for magnetisation of the air gap, but also of the iron paths in the teeth (teeth heights h_{ds}, h_{dr}) – and partly also of the stator and the rotor joke.

$$V_s = H_\delta \cdot \delta + H_{ds} \cdot h_{ds} + H_{dr} \cdot h_{dr} \Rightarrow B_\delta < \mu_0 \frac{V_s}{\delta} \sim I_{s0} \tag{6.32}$$

From (6.32) it can be derived, that the magnetic field in the air gap B_δ and hence the internal voltage U_h increase sub-proportionally with increasing no-load current I_{s0}, which results in a curved **no-load characteristic** $U_h(I_{s0})$ (Fig. 6.16). The tangent to the curve (dashed **"air gap line"** in Fig. 6.16) corresponds to the unsaturated machine, where only the air gap has to be magnetised. The stator voltage equation at no-load (6.33) contains the **saturation dependent magnetising reactance** $X_{h,sat}$ that is **smaller** than the non-saturated magnetising reactance X_h, which was derived in Chapter 4.

$$\underline{U} = \left(R_s + jX_{s\sigma}\right)\underline{I}_{s0} + \underline{U}_h = \left(R_s + j(X_{s\sigma} + X_{h,sat})\right)\underline{I}_{s0} \tag{6.33}$$

$$U_h = X_{h,sat}(I_{s0})I_{s0} < X_h I_{s0} \tag{6.34}$$

At load, the air gap field is excited both from the stator and the rotor current, and I_{s0} in (6.33) has to be replaced by the magnetising current I_m. Often, the circle diagram is constructed for a machine that is saturated at $U_h = U_N$ with an approximately load **in**dependent magnetising reactance $X_{h,sat}$. Hence, X_h of Chapter 5 has only to be replaced by $X_{h,sat}$. This is only acceptable for small values of the slip s up to breakdown slip, because the magnetising current almost equals the magnetising current at no-load.

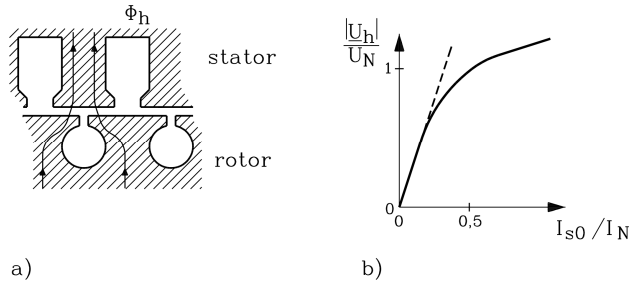

Fig. 6.16: Saturation of the teeth due to the magnetising field: a) magnetising field path, b) **"no-load characteristic"**

c) Influence of the Leakage Field Saturation:
Fig. 6.15b shows that, at s = 1, the magnetic field is displaced from the rotor to the air gap due to current displacement. **"Flux compensation"** occurs where rotor and stator current are almost opposite: $s = 1 : \underline{I}_s \approx -\underline{I}'_r$. Many flux lines pass from the stator to the rotor teeth tips and do not enter the rotor any further. They generate a leakage flux that goes **zigzag** in the air gap from one stator tooth tip to the next rotor tooth tip to the following stator tooth tip and so on (**"zigzag leakage"**). This is indicated schematically in Fig. 6.17a. This leakage flux occurs only at high values of the slip s, where it forces the tooth tips to saturate. Thereby, the leakage inductances are reduced.

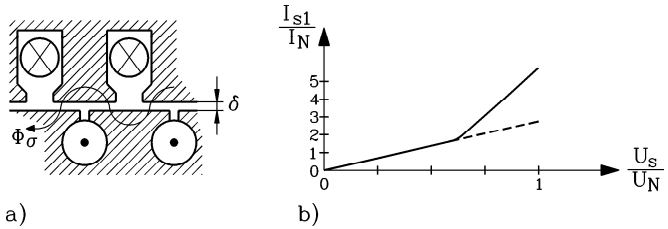

Fig. 6.17: Saturation of the leakage paths at s = 1 due to zigzag leakage: a) path of leakage flux, b) "short-circuit characteristic"

$$s = 1 : \underline{U} \cong \left[\left(R_s + R'_r\right) + j\left(X_{s\sigma,sat} + X'_{r\sigma,sat}\right)\right]\underline{I}_s \tag{6.35}$$

$$X_{s\sigma,sat} < X_{s\sigma}\,,\ X'_{r\sigma,sat} < X'_{r\sigma} \tag{6.36}$$

Therefore, at breakaway, the current does not increase linearly with the voltage, but super-proportionally, as can be seen from the **"short-circuit characteristic"** shown in Fig. 6.17b.

The effect of the zigzag leakage on the shape of the current locus diagram is the same as the effect of current displacement. A reduction of the leakage inductance causes "inflation" of the circle diagram at high slip values (see Fig. 6.14).

d) Influence of Field Harmonics:
In Chapters 5 and 6, only the **fundamental** of the magnetic field was considered for the calculation of the torque of the induction machine. The stator and rotor field harmonics as

discussed in Chapters 3 and 4 generate additional, parasitic torque components. They cause **asynchronous harmonic torque components** that result in saddles of the $M(n)$-characteristic ("torque saddles") and in pulsating (alternating) torque components at certain speed (**synchronous harmonic torque**). Squirrel-cage machines are much more sensitive to these effects of harmonic effects than slipring induction machines, because the cage can be induced by any rotating field with any pole number. On the contrary, the three phase rotor winding of slipring machines is only induced by field harmonics with those pole numbers that are generated by the winding itself. In the case of symmetric three phase windings, these are – beside the fundamental – fields with 5, 7, 11, 13 etc. times the pole number. Therefore, effects of harmonics are less critical in the case of slipring machines. Details of these effects – that are often connected with strong magnetic noise (**"siren sound"**) – and their minimisation are discussed in the lecture *"Motor Development for Electric Drive Systems"*.

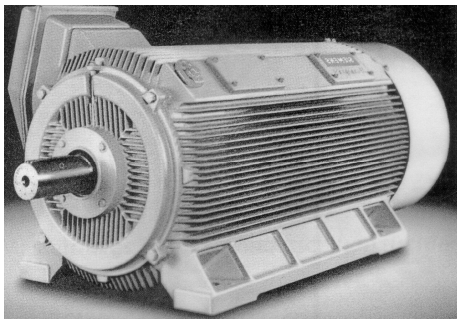

Fig. 6.18: Totally enclosed, fan cooled induction machine 1.5 MW with slipring cage and housing with cooling fins for surface air cooling, used as generator in wind power plants

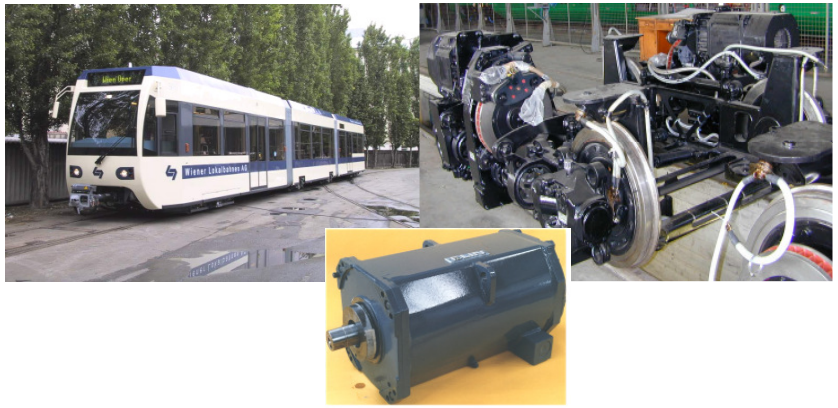

Fig. 6.19: Centre: Inverter-fed, speed variable squirrel cage induction motor (50 kW) with water jacket cooling as drive for street cars (left above). Motor is integrated in the 4-wheel bogie (right above) via gear box to adjust high motor speed (= small motor torque = small motor) to low wheel-set speed. By arranging motor and gear box to right and left side in bogie, no trans-axle between wheel-sets is needed, leaving space for the cabin in between. Thus a "low floor" street car is designed.